Particle & Particle Systems Characterization
www.particle-journal.com

Estimation of Temperature Homogeneity in MEMS-Based Heating Nanochips via Quantitative HAADF-STEM Tomography

*Qiongyang Chen, Alexander Skorikov, Jessi E. S. van der Hoeven, Alfons van Blaaderen, Wiebke Albrecht, H. Hugo Pérez-Garza, and Sara Bals**

Sample holders for transmission electron microscopy (TEM) based on micro-electro-mechanical systems (MEMS) have recently become popular for investigating the behavior of nanomaterials under in situ or environmental conditions. The accuracy and reproducibility of these in situ holders are essential to ensure the reliability of experimental results. In addition, the uniformity of an applied temperature trigger across the MEMS chip is a crucial parameter. In this work, it is measured the temperature homogeneity of MEMS-based heating sample supports by locally analyzing the dynamics of heat-induced alloying of Au@Ag nanoparticles located in different regions of the support through quantitative *fast* high-angle annular dark-field scanning TEM tomography. These results demonstrate the superior temperature homogeneity of a microheater design based on a heating element shaped as a circular spiral with a width decreasing outwards compared to a double spiral-shaped designed microheater. The proposed approach to measure the local temperature homogeneity based on the thermal properties of bimetallic nanoparticles will support the future development of MEMS-based heating supports with improved thermal properties and in situ studies where high precision in the temperature at a certain position is required.

1. Introduction

Transmission electron microscopy (TEM) is a powerful tool for characterizing the microstructure and composition of (nano)materials. By combining TEM with various stimuli provided by sample carriers, in situ observations become possible. In situ TEM can be used to directly observe the dynamic behavior of nanomaterials under different conditions at high resolution.[1,2] One of the most powerful technologies for in situ sample holders is based on micro-electro-mechanical systems (MEMS), which can provide a variety of stimuli such as heating, biasing, and gas or liquid environments.[2–5] For example, in situ microheaters or "nanochips" enable TEM observations at temperatures up to 1300°C with high stability, controllable drift rate, and the possibility to rapidly and accurately change temperature.[6]

Such heating nanochips enable in situ TEM investigations to understand morphological restructuring or chemical composition changes of materials at different temperatures. It is crucial to investigate whether materials can maintain their morphology and chemical composition to ensure their stability and efficacy under their application conditions. For example, bimetallic nanoparticles are known for their unique plasmonic, photothermal, and catalytic properties, such as Au/Pd, Au/Pt, and Au/Ag nanoparticles; properties that strongly depend on the distribution

Q. Chen, A. Skorikov, W. Albrecht, S. Bals
EMAT
University of Antwerp
Groenenborgerlaan 171, Antwerp B-2020, Belgium
E-mail: sara.bals@uantwerpen.be
Q. Chen, A. Skorikov, W. Albrecht, S. Bals
NanoLab Center of Excellence
University of Antwerp
Groenenborgerlaan 171, Antwerp B-2020, Belgium
A. Skorikov
Computational Imaging group
Centrum Wiskunde and Informatica (CWI)
Science Park 123, Amsterdam 1098 XG, Netherlands
J. E. S. van der Hoeven, A. van Blaaderen
Soft Condensed Matter
Debye Institute for Nanomaterials Science
Utrecht University
Princetonplein 5, Utrecht 3584 CC, Netherlands
J. E. S. van der Hoeven
Materials Chemistry and Catalysis
Debye Institute for Nanomaterials Science
Utrecht University
Universiteitsweg 99, Utrecht 3584 CG, Netherlands
H. H. Pérez-Garza
DENSsolutions B.V.
Informaticalaan 12, Delft 2628 ZD, Netherlands

The ORCID identification number(s) for the author(s) of this article can be found under https://doi.org/10.1002/ppsc.202300070

DOI: 10.1002/ppsc.202300070

of the two metals, which are subject to change at higher temperatures.[7–12] Recently, electron tomography was combined with a MEMS-based heating sample holder to investigate structural and compositional changes of anisotropic Au, Au/Pd, and Au/Ag nanoparticles at high temperatures.[13–15] In these studies, electron tomography in high-angle annular dark-field scanning transmission electron microscopy (HAADF-STEM) mode was used to accurately sample the 3D transformations of the nanoparticles as a function of heating time and temperature. Obviously, the temperature homogeneity and stability of microheaters are of great importance when performing a quantitative interpretation of such in situ TEM experiments.

For a typical in situ heating TEM experiment, nanoparticles are drop-casted onto the nanochip and heated to a specific temperature by heat transfer between the microheater and the particles. The temperature of the nanochips is controlled using a four-point probe configuration as a part of a closed-loop feedback system. Within this configuration, two contacts deliver the electrical current that induces Joule heating, whereas the remaining two contacts are used to measure the microheater's resistance, which linearly depends on temperature. Hereby, the temperature-resistance relationship needs to be calibrated externally, typically using Raman spectroscopy[16] or infrared pyrometry.[1] One significant problem of temperature calibrations based on Raman spectroscopy and infrared pyrometry is that they cannot track the actual temperature of, e.g., heated nanoparticles in different regions of the nanochip. Indeed, these temperature measurements are performed at a scale of hundreds of nanometers to micrometers, which is too large to track the local temperature on the level of individual nanoparticles. In combination with the temperature inhomogeneity that can be intrinsically present in a microheater, local differences in the heat transfer efficiency from the chip to the nanoparticles can lead to discrepancies between the estimated and real temperatures of nanoparticles on the nanochip.[17] Direct, local methods for nanoparticle temperature measurement in TEM are thus of great importance during in situ heating experiments. In the past, several such methodologies have been proposed based on phase transformations,[18] magnetic effect transitions,[19] amorphous to crystalline transformation,[20,21] or luminescence thermometry.[22–25] Gao et al.[26] and Gong et al.[27] measured the temperature of localized regions of nanosystems by tracking the thermal expansion of metal inside a carbon nanotube at elevated temperatures. Also, electron energy-loss spectroscopy[28–31] and electron diffraction approaches[32–35] were suggested for local temperature measurements in TEM.

Here, we propose an alternative method to accurately measure temperature differences in various regions of MEMS-based heating nanochips at the sub-micron scale. The approach involves analyzing the dynamics of elemental diffusion within individual nanoparticles based on in situ heating HAADF-STEM tomography experiments. Our method utilizes the fact that the rate of elemental diffusion strongly depends on the temperature. This allows us to use bimetallic nanoparticles as probes of the local temperature by measuring the rate of their heating-induced alloying. In this work, we employ this method to investigate possible thermal gradients within the microheaters and make a comparison between different designs of heating nanochips in terms of temperature homogeneity.

2. Results and Discussion

Au@Ag core-shell nanorods were obtained by a seed-mediated method which was reported by van der Hoeven et al.[36] A mesoporous silica shell was present to minimize the reshaping of the nanoparticles upon heating.[37] Figure S1, Supporting Information shows a HAADF-STEM image and an EDX elemental map of a representative Au@Ag core-shell nanorod.

These samples were studied by in situ heating electron tomography, using the DENSsolutions Wildfire S5 system, which enabled us to follow the alloying process in 3D. Following the procedure used in the previous work of Skorikov et al,[15] we performed in situ experiments during which we heated the sample inside the TEM and let the sample cool back to room temperature after specific heating intervals to collect tilt series for subsequent 3D reconstruction. In this manner, we avoided changes within the nanoparticles during a single tilt series acquisition. To reduce the total acquisition time and electron dose, we used *fast* electron tomography acquisition, allowing us to acquire the tilt series within 6 min for a tilt range of ±72°.[13] During the acquisition of the tilt series, the holder was rotated continuously and intermediate manual refocusing and repositioning were performed while tilting. For each data set, a 3D reconstruction was calculated using the expectation-maximization algorithm.[38,39] Since the intensities in the HAADF-STEM scale with the atomic number Z, the grey levels in the 3D reconstruction can be used to quantify the local composition of the nanorods.[15] Compared to 2D projection HAADF-STEM images, which contain both thickness and elemental information, the contrast in the orthoslices through a 3D reconstruction only depends on the elemental distribution inside the nanoparticles.[40] Therefore, the voxel intensities extracted from the 3D reconstruction can be used to retrieve the 3D elemental distribution (Figure S2a–c, Supporting Information). Furthermore, the spread of the voxel intensities at each heating step follows the dynamics of the underlying alloying, starting from two separate peaks in the intensity histogram corresponding to Au (core) and Ag (shell) of the initial core-shell nanorod. These voxel intensities gradually transform into one peak corresponding to an intermediate grey level that represents the completely alloyed material. Therefore, this spread can be used to quantify the alloying degree of nanoparticles at different time steps (Figure S2d,e, Supporting Information).

In this work, we used the alloying dynamics of Au@Ag core-shell nanorods as a probe to investigate possible temperature differences between different windows on a nanochip (**Figure 1**a). To exclude the influence of size, shape, aspect ratio, and composition on the dynamics of alloying and to ensure that differences in diffusion coefficients extracted from in situ heating experiments were a function of temperature only, we selected nanorods with similar structural parameters and composition. By tracking the alloying dynamics of these nanorods, it became possible to investigate differences in temperature for different regions of a nanochip.

We used the methodology explained above to analyze the temperature homogeneity of two different types of DENSsolutions Wildfire nanochips: the double spiral-shaped microheater (old generation of nanochips, which is no longer in production, nor commercially available) (Figure 1b) and the circular spiral-shaped microheater (the current and optimized nanochip design that is

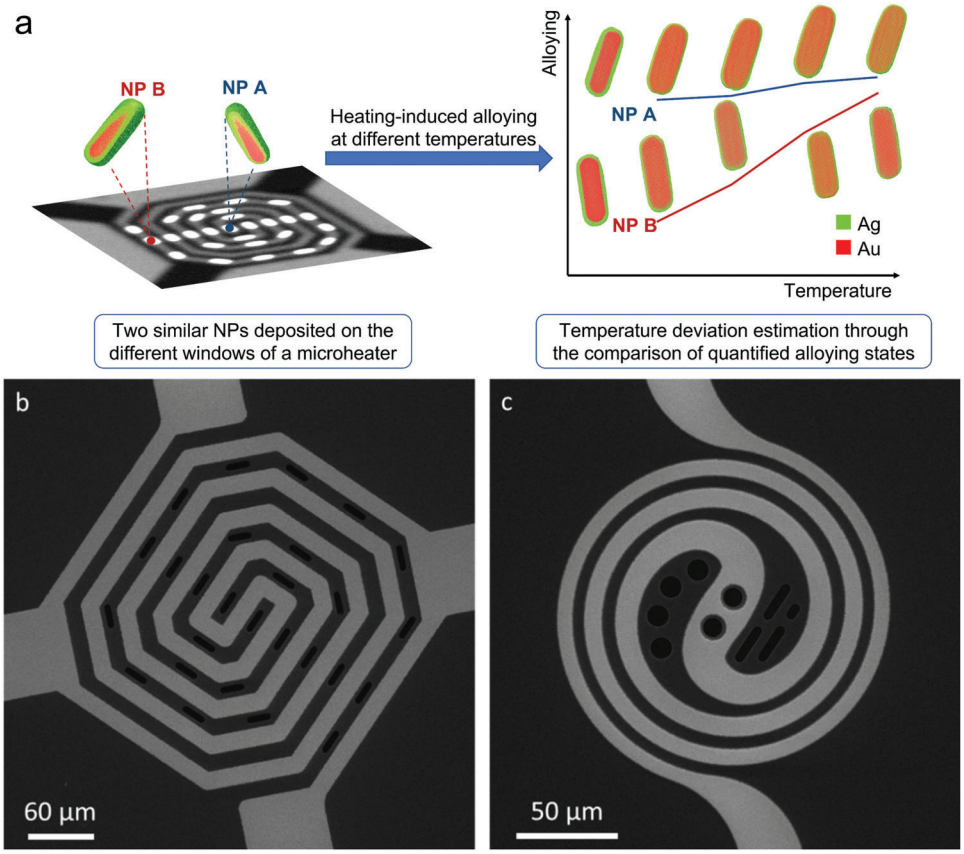

Figure 1. a) Schematic diagram of the method for estimating local temperature distribution. Overview SEM images of different designed DENSsolutions Wildfire nanochips: b) the double spiral-shaped DENSsolutions Wildfire nanochip. c) the circle spiral-shaped DENSsolutions Wildfire nanochip.

commercially available) (Figure 1c). For both designs, we compared two windows, one near the middle of the nanochip and another near the edge, since the largest temperature gradient within the nanochips occurs in this direction.[6,16] Details of the nanoparticles used in our study can be found in Tables S1 and S2, Supporting Information.

The nanochip was heated to a nominal value of 400 °C to induce alloying.[37] Next, the temperature was increased with intervals of 10 °C and samples were kept at a given temperature for 2 min. After each interval, samples were rapidly cooled to 25 °C, and *fast* tomography tilt series were acquired. In this manner, we investigated the alloying degree of the nanoparticles at four different nominal temperatures ranging from 400 °C to 430 °C. For each particle, we obtained 3D reconstructions at these temperatures as well as an additional one at room temperature (RT) before alloying as a reference. **Figures 2** and **3** show the results obtained for the two different nanochip designs. By inspecting orthoslices through the quantified 3D HAADF-STEM reconstructions of nanoparticles (Figure 2b,c and Figure 3b,c), progressive alloying upon heating is observed. The dynamics of the alloying process are reflected in the distributions of the voxel intensities at different temperatures. Indeed, at RT, two peaks at different voxel intensities can be distinguished, corresponding to the core and shell of the nanoparticles. During alloying, these peaks merge into a single peak at an intensity in between both original peaks.

For the double spiral-shaped nanochip (i.e., the old and discontinued design), two nanoparticles were placed in two windows with a distance of ≈90 µm between them, which represents the maximum geometric separation observed on the nanochip. The nanoparticle in the middle window shows a uniform compositional distribution (corresponding to the highly alloyed state of the particle) after heating above 400 °C. Indeed, compared to the nanoparticle at room temperature, as the alloying process evolved, the two peaks of the Ag and Au corresponding to the unalloyed state transferred to one single peak in the histogram. Figure 2b shows that the Au and Ag atoms were close to completely interfused between the shell and the core of the nanoparticle already at a nominal value of 400 °C. However, for the nanoparticle located on the window at the edge of the same double spiral-shaped nanochip, the dynamics of alloying were different. Figure 2c shows that a clear shoulder on the left side of the peak is present in the histograms for 400 °C and 410 °C and a single peak only appears at 420 °C. The difference in alloying behaviors between the two nanoparticles indicates potential local temperature deviation in the different regions of the nanochip.

Next, we performed the same experiment for the circular spiral-shaped microheater (i.e., the current and optimized design). Again, two nanoparticles with similar size, shape, aspect ratio, and composition were selected, of which one was located on the central window and the other on a window near the edge of the nanochip. The distance between these two windows was

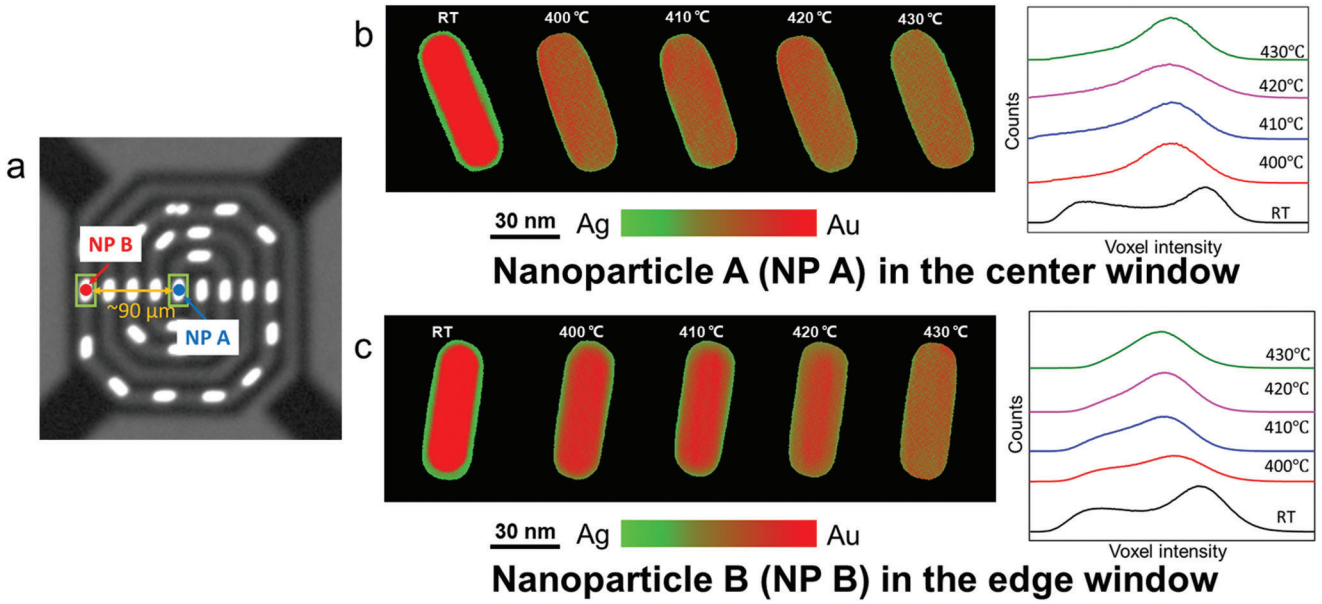

Figure 2. a) TEM image of the double spiral-shaped DENSsolutions Wildfire nanochip. Two nanoparticles with similar size, shape, aspect ratio, and composition (NP A and NP B) located on a window near the center and near the edge, respectively, are selected. b) and c) Slices through the 3D compositional distribution in NP A and NP B, respectively, show different dynamics of alloying behavior, which is also clear from the evolution of the histogram of voxel intensities within the nanoparticles.

≈35 µm. From Figure 3, the evolution of the elemental distribution within the nanoparticles and the corresponding intensity histograms show that the alloying dynamics of the nanoparticles located on the two windows are comparable.

To assess the local temperature difference on the nanochips in a more quantitative manner, we calculated the degree of alloying for each nanoparticle at different temperatures as explained in the Supporting Information. As can be seen from **Figure 4**, a discrepancy in the alloying dynamics was found for nanoparticles deposited on a double spiral-shaped microheater, in agreement with the observations in Figure 2. From Figure 4a, it is clear that the nanoparticle in the middle window displays a higher degree

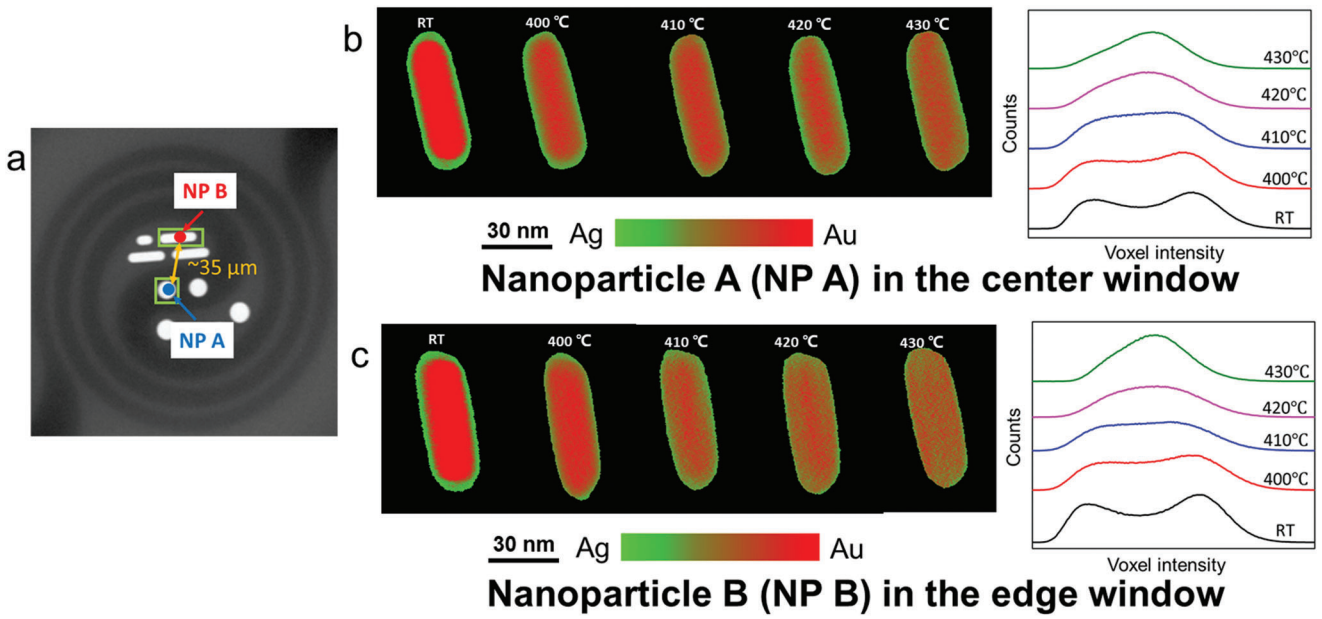

Figure 3. a) TEM image of the circular spiral-shaped DENSsolutions Wildfire nanochip. Two nanoparticles with similar size, shape, aspect ratio, and composition (NP A and NP B) located on a window near the center and near the edge, respectively, are selected. b) and c) Slices through the 3D compositional distribution in NP A and NP B, respectively, show the same dynamics of alloying behavior, which is also clear from the evolution of the histogram of voxel intensities within the nanoparticles.

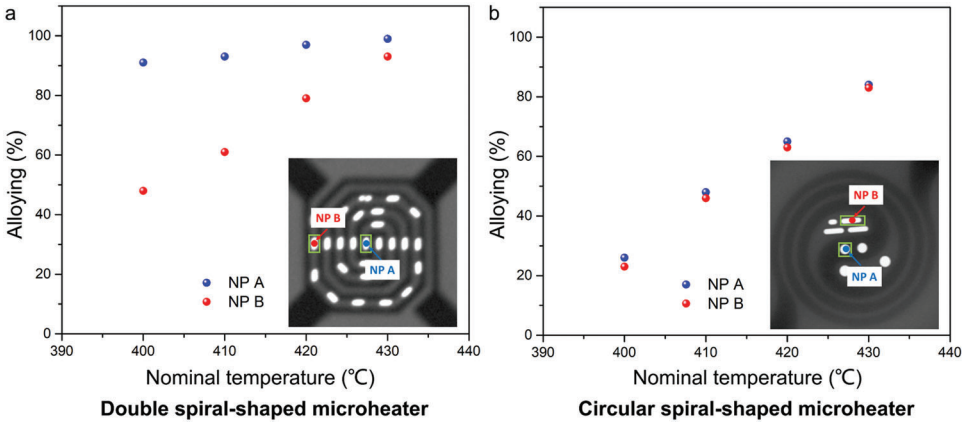

Figure 4. Comparison of the quantified dynamics of alloying for the nanoparticles located at different windows in a) the double spiral-shaped microheater and b) the circular spiral-shaped microheater estimated from the 3D reconstructions of the compositional distribution based on fast HAADF-STEM tomography.

of alloying already after heating at a nominal value of 400 °C for 2 min. However, the nanoparticle located at the window near the edge demonstrates slower alloying dynamics, where the degree of alloying gradually increases from 400 °C to 430 °C. It should be noted that the alloying state of NP B at 420 °C is still lower than that of NP A at 400 °C.

On the other hand, the circular spiral-shaped microheater yields much better temperature homogeneity (Figure 4b), and consistent alloying behavior of the nanoparticles was observed. This observation indicates that the circular spiral-shaped nanochip yields superior temperature homogeneity. This clear improvement was expected since the line width of the metal lines of the heating spiral was designed to gradually increase from the edge towards the center of the microheater. As can be observed in the paper published by van Omme et al,[6] the increase in the width of the heater provides a decrease of resistance towards the middle point of the microheater, resulting in a more intense Joule heating in the outer metal lines of the spiral in comparison to its central part. This compensates for the thermal gradient that otherwise occurs in the double spiral-shaped nanochip with a fixed width of the heating spiral, which is caused by a more efficient heat dissipation at the edges of the chip. Because of the high homogeneity over the entire microheater's area, the circular spiral-shaped design provides a larger surface for investigating heat-induced processes in nanomaterials with an accurate temperature calibration.

It is interesting to quantify the temperature difference that is present for the different locations on the different nanochip designs. In order to reach this goal, we first calculate the values of the diffusion coefficient for the Au–Ag nanoparticles at different temperatures and then employ the Arrhenius equation to calculate the difference in the temperature perceived by the NPs. Throughout the heating process, the nanoparticles were heated in 10 °C steps from the nominal temperature of 400 °C to 430 °C and kept at each given temperature for 2 min. To estimate the diffusion coefficients for the NPs at different temperatures, we performed 3D alloying simulations based on Fick's law. At each interval, the simulation was initialized with the measured 3D elemental distribution, and the value of the diffusion coefficient was numerically optimized to match the next measured state of alloying after 2 min of heating (see also Experimental Section and our previous work[15]).

The results of this analysis are shown in **Figure 5**. For the NPs in the double spiral-shaped microheater, the obtained values of the diffusion coefficients for the nanoparticle in the center window (NP A, Figure 5a) are significantly higher than that of the nanoparticle in the edge window (NP B, Figure 5b) for all intervals. On the other hand, the NPs in the circle spiral-shaped microheater demonstrate consistent diffusion coefficients and similar alloying progress as shown in Figure 5c,d. In the latter case, the obtained diffusion coefficients also agree well with the reported literature values. Although our results were observed at around 400 °C, the fitting curve of the diffusion coefficients can be used for estimating the activation energy and the diffusion coefficients at other temperatures as shown in Table S3, (Supporting Information for 450 °C. The nanoparticles in our study show similar activation energy as bulk materials[41,42] (about $1.3*10^{24}$ eV/mol). The diffusion coefficients predicted by our method also fit well to tabulated bulk values and other referenced Au@Ag NPs[15,43] at 450 °C.

To determine the temperature deviation between the particles, we analyzed the temperature dependence of the calculated diffusion coefficients by applying the Arrhenius equation. For one of the particles on a chip (e.g., NP A), nominal temperatures were assumed, and for the other NP (e.g., NP B) a temperature difference was introduced as an additional parameter:

$$D_A\ (T) = D_0\, e^{-\frac{Q}{RT}} \tag{1}$$

$$D_B\ (T) = D_0\, e^{-\frac{Q}{R(T+\Delta T)}} \tag{2}$$

where D_A and D_B are temperature-dependent diffusion coefficients [m^2/s] for NP A and NP B, respectively, D_0 is the diffusion coefficient for when the temperature is so high that the activation energy can be neglected [m^2/s], Q is the activation energy for diffusion [J/mol], R is the universal gas constant [8.314 J/ (mol *K)], T is the nominal temperature [K] of the chip, and ΔT is the modeled temperature difference between NP A and NP B. Next, the unknown parameters D_0, Q and ΔT were determined

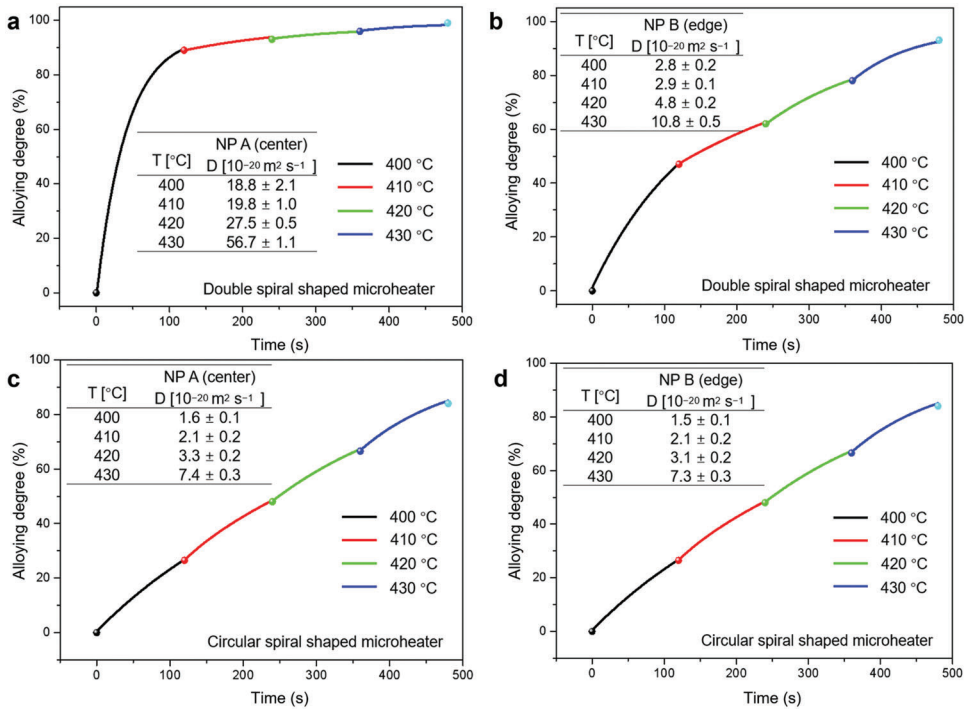

Figure 5. The progress of alloying was quantified from the experimental data (points) and simulation results with different diffusion coefficients at different temperatures (solid lines). Comparison of diffusion simulations and experiments for the nanoparticles located at different windows in a,b) the double spiral-shaped microheater and c,d) the circular spiral-shaped microheater.

by least squares fitting of the experimentally measured diffusion coefficients for NP A and NP B (see the Experimental Section). Although we arbitrarily assume that the temperature of NP A follows the nominal temperature of the nanochip, the results of the fitting and the determined values of ΔT are insensitive to whether NP A or NP B is chosen as a reference. **Figure 6** demonstrates the results of the fitting and the determined values of ΔT for double spiral and circular spiral-shaped microheaters. It can be observed, that for the double spiral-shaped design (Figure 6a), there is a significant shift between the experimentally measured values of the diffusion coefficient for NP A and NP B, which corresponds to a temperature difference of 34 ± 8 °C. This value is an indication of the discrepancy between the temperature on different windows of the double spiral-shaped microheater. On the other hand, no significant temperature discrepancy was detected based on the diffusion coefficients of NP A and NP B located on the microheater with the circular spiral-shaped design (Figure 6b). These results corroborate our previous observation on improved temperature homogeneity of the newer microheater design. Importantly, the value of the temperature discrepancy measured by the proposed method can be used in simulations to estimate the magnitude of differences in the relevant physicochemical processes (e.g., rates of nanoparticle reshaping and alloying) for experiments where the older microheater design was used.

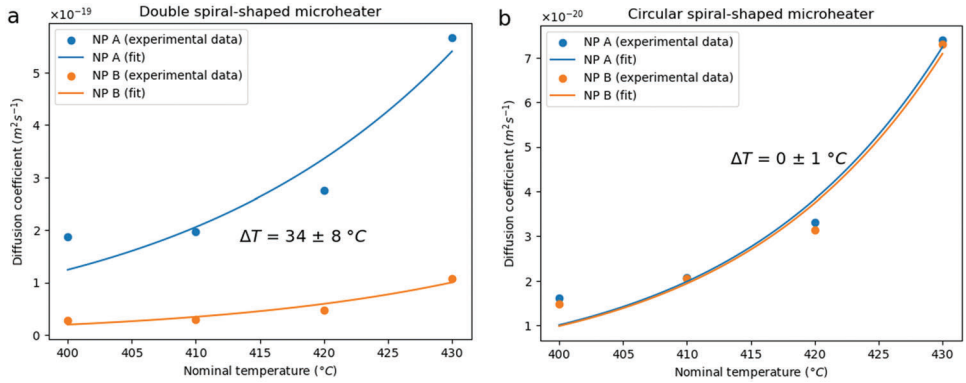

Figure 6. Experimentally measured values of diffusion coefficients and they fit with Arrhenius equation for NP A and NP B located on different windows of the double spiral a) and circular spiral-shaped b) microheaters. Indicated temperature difference ΔT was determined as a fitting parameter in the model, and its uncertainty represents the standard deviation of the estimated value.

3. Conclusion

We estimated the local temperature deviation in microheaters for in situ TEM studies by following the dynamics of bimetallic nanoparticles alloying based on quantitative analysis of HAADF-STEM-based 3D reconstructions. By comparing the results for two different designs of nanochips, we conclude that the circular spiral-shaped microheater yields superior temperature homogeneity. Such high homogeneity over the entire area of the microheater drastically improves the available viewing area for accurate quantitative in situ TEM heating experiments. Our proposed method can quantify highly localized temperature inhomogeneities (based on the size of the NPs used). In addition, it is a versatile tool in all in situ heating studies, where it is crucial to determine minute temperature differences in different locations. By using nanoparticles as shown here, such temperature differences can even be quantified on sub-micrometer length scales, which among other things enables studies on local temperature resistances in nanoscale devices.

4. Experimental Section

Sample Description: The synthesis of the mesoporous silica-coated Au-core Ag-shell nanorods was carried out using the multi-step colloid synthesis approach described in detail in the work of van der Hoeven et al.[36] In short, the synthesis steps comprised i) gold nanorod synthesis, ii) mesoporous silica coating, iii) oxidative etching, and iv) Ag overgrowth. The procedure of *Ye* et al. was used to synthesize the gold nanorods.[44] The seed solution consisted of 10 mL 0.10 M CTAB and 51 µL 50 mM $HAuCl_4$ and 1.0 mL 0.0060 M $NaBH_4$. The growth solution contained 7.0 g cetrimonium bromide (CTAB) and 1.24 g sodium oleate, 250 mL Milli-Q H_2O, 250 mL 1.0 mM $HAuCl_4$, 7.2 mL 10 mM $AgNO_3$, 2.1 mL HCl (37 wt%, 12.1 M), 1.25 mL 0.064 M ascorbic acid and 0.80 mL seed solution. The resulting rods were washed with H_2O and redispersed in 175 mL 1.5 mM CTAB water (LSPR peak position = 853 nm). The mesoporous silica coating procedure originates from the work of *Gorelikov* et al.[45] The growth solution contained 175 mL 1.5 mM CTAB solution, 1.75 mL 0.1 M NaOH, and 1.575 mL 0.90 M TEOS in EtOH. The resulting Au@SiO_2 NRs were washed with water and ethanol (EtOH) and redispersed in 210 mL methanol (MeOH) for subsequent oxidative etching.[36] The etching solution contained 100 mL mesoporous silica-coated AuNRs in MeOH (LSPR peak position = 838 nm), 2.0 mL HCl (37 wt%, 12.1 M), and 2.0 mL 50 mM H_2O_2 in MeOH. The etching was carried out at 60°C for 26 minutes (LSPR peak position = 694 nm), followed by quenching with 100 mL ice-cold MeOH. The etched rods were washed with and redispersed in 120 mL H_2O. Finally, the Ag shell was grown[36,46] in a reaction mixture containing 120 mL aqueous rod dispersion, 1.5 mL 0.10 M HCl, 6.6 mL 5.0 mM $AgNO_3$, and 6.6 mL 20 mM ascorbic acid in water. After 20 min, the rods were washed with water and EtOH and stored in EtOH in the dark at 4 °C to prevent oxidation and dissolution of the Ag shell.

Heating, Tomographic Series Acquisition, and Reconstruction: All experiments were performed using a ThermoFisher Tecnai Osiris electron microscope operated at 200 kV in HAADF-STEM mode, using a DENSsolutions tomographic heating holder with a MEMS-based heating nanochip. We used two types of Wildfire nanochip designs with high-temperature precision and uniformity for local temperature measurement in TEM. Two nanoparticles with similar structural parameters and compositions were located on each chip: one on the central window and one on a window at the edge of the chip (the distance between the windows is approximately 90 µm for the old nanochip design and around 35 µm for the new design). Tilt series of nanoparticles for 3D reconstruction were acquired between −72° and 72° using the *fast* tomography method, as described elsewhere.[13] The acquired tilt series were aligned using cross-correlation and 3D reconstructions were obtained using the Expectation-Maximization (EM) algorithm,[38] as implemented in the Astra Toolbox[39] for MATLAB 2018a.

Quantification of Alloying Degree: The characterization of the 3D elemental distributions and the quantification of the degree of alloying are based on our previous work[15] and also described in detail in the Supporting Information.

Alloying Simulations: 3D alloying simulations based on the homogeneous isotropic Fick's law were used for obtaining diffusion coefficients of nanoparticles at different temperatures:

$$\frac{dC}{dt} = D\,(\Delta * C) \tag{3}$$

where C = C(x, y, z, t) is the 3D elemental distribution evolving in time, D is the diffusion coefficient and * is a spatial convolution operation. Δ is the Laplace operator. Throughout the heating process, the nanoparticles were heated in a stepwise manner and remained at each given temperature for the same amount of time. At each interval, the simulation was initialized with the measured 3D elemental distribution, and the value of the diffusion coefficient was numerically optimized to match the next measured state of alloying after 2 min of heating. Moreover, the "missing wedge" effects and blurring artifacts in the simulated reconstructions at each heating step were incorporated in the same way as explained above for the simulations of the perfectly alloyed states of the nanoparticles based on our previous work.[15]

Quantification of the Relative Temperature Difference: To quantify the relative temperature difference, the measured values of diffusion coefficient for two particles on a given microheater were fitted using the Arrhenius equation. For NP A, nominal temperatures were assumed (Equation 1) and for NP B, an additional parameter ΔT representing temperature difference with respect to NP A was introduced (Equation 2). Hereby, diffusion activation energy Q and preexponential factor D_0 were assumed to be the same for both nanoparticles, which is justified by their similar size and composition. Next, parameters Q, D_0 and ΔT were obtained via non-linear least squares fitting performed using the Levenberg–Marquardt method implemented in SciPy 1.9 software package.[47] We note that the obtained values for the fitting parameters did not differ significantly if either NP A or NP B was assumed to follow the nominal temperature of the microheater. The systematic offset between the datapoints and the fit observed at all plots (e.g., the last point always lying above the fitted graph) is most likely related to the effect we observed before in our previous work:[15] during the last stages of heating particles alloy faster than expected from modeling based purely on Fick's law because of particle deformation (see Figure S3, Supporting Information).

Supporting Information

Supporting Information is available from the Wiley Online Library or from the author.

Acknowledgements

This project was funded from the European Commission and The Marie Skłodowska-Curie Innovative Training Network MUMMERING (Grant Agreement no. 765604)

Conflict of Interest

The authors declare no conflict of interest.

Data Availability Statement

The data that support the findings of this study are available from the corresponding author upon reasonable request.

Keywords

alloying dynamics, fast HAADF-STEM tomography, in situ microheater, temperature distribution

Received: May 10, 2023
Revised: August 22, 2023
Published online:

[1] L. F. Allard, W. C. Bigelow, M. Jose-Yacaman, D. P. Nackashi, J. Damiano, S. E. Mick, *Microsc. Res. Tech.* **2009**, *72*, 208.
[2] L. Mele, S. Konings, P. Dona, F. Evertz, C. Mitterbauer, P. Faber, R. Schampers, J. R. Jinschek, *Microsc. Res. Tech.* **2016**, *79*, 239.
[3] C. Gong, A. W. Robertson, K. He, G. Do Lee, E. Yoon, C. S. Allen, A. I. Kirkland, J. H. Warner, *ACS Nano* **2015**, *9*, 10066.
[4] T. Altantzis, I. Lobato, A. de Backer, A. Béché, Y. Zhang, S. Basak, M. Porcu, Q. Xu, A. Sánchez-Iglesias, L. M. Liz-Marzán, G. van Tendeloo, S. van Aert, S. Bals, *Nano Lett.* **2019**, *19*, 477.
[5] A. Ianiro, H. Wu, M. M. J. van Rijt, M. P. Vena, A. D. A. Keizer, A. C. C. Esteves, R. Tuinier, H. Friedrich, N. A. J. M. Sommerdijk, J. P. Patterson, *Nat. Chem.* **2019**, *11*, 320.
[6] J. T. van Omme, M. Zakhozheva, R. G. Spruit, M. Sholkina, H. H. P. Garza, *Ultramicroscopy* **2018**, *192*, 14.
[7] C. J. Desantis, S. E. Skrabalak, *Langmuir* **2012**, *28*, 9055.
[8] S. Hou, X. Hu, T. Wen, W. Liu, X. Wu, *Adv. Mater.* **2013**, *25*, 3857.
[9] J. K. Edwards, B. E. Solsona, P. Landon, A. F. Carley, A. Herzing, C. J. Kiely, G. J. Hutchings, *J. Catal.* **2005**, *236*, 69.
[10] H. Liao, A. Fisher, Z. J. Xu, *Small.* **2015**, *11*, 3221.
[11] B. Zugic, L. Wang, C. Heine, D. N. Zakharov, B. A. J. Lechner, E. A. Stach, J. Biener, M. Salmeron, R. J. Madix, C. M. Friend, *Nat. Mater.* **2017**, *16*, 558.
[12] W. Albrecht, J. E. S. van der Hoeven, T. S. Deng, P. E. de Jongh, A. van Blaaderen, *Nanoscale* **2017**, *9*, 2845.
[13] H. Vanrompay, E. Bladt, W. Albrecht, A. Béché, A. Sánchez-iglesias, L. M. Liz-marzán, S. Bals, S. Sebastian, *Nanoscale* **2018**, *10*, 22792.
[14] W. Albrecht, E. Bladt, H. Vanrompay, J. D. Smith, S. E. Skrabalak, S. Bals, *ACS Nano* **2019**, *13*, 6522.
[15] A. Skorikov, W. Albrecht, E. Bladt, X. Xie, J. E. S. van der Hoeven, A. van Blaaderen, S. van Aert, S. Bals, *ACS Nano* **2019**, *13*, 13421.
[16] H. H. Pérez-Garza, D. Morsink, J. Xu, M. Sholkina, Y. Pivak, M. Pen, S. van Weperen, Q. Xu, *2016 IEEE 11th Annu. Int. Conf. Nano/Micro Eng. Mol. Syst.* **2016**, 85, https://doi.org/10.1109/NEMS.2016.7758206.
[17] R. G. Spruit, J. T. van Omme, M. K. Ghatkesar, H. H. P. Garza, *J. Microelectromech. Syst.* **2017**, *26*, 1165.
[18] J. Bonneaux, M. Guymont, *Intermetallics* **1999**, *7*, 797.
[19] C. J. Martin, J. D. Boyd, *J. Phys. E: Sci. Instrum.* **1973**, *6*, 21.
[20] R. Sinclair, M. A. Parker, *Nature* **1986**, *322*, 531.
[21] E. A. Stach, R. Hull, J. C. Bean, K. S. Jones, A. Nejim, *Microsc. Microanal.* **1998**, *4*, 294.
[22] R. G. Geitenbeek, P. T. Prins, W. Albrecht, A. van Blaaderen, B. M. Weckhuysen, A. Meijerink, *J. Phys. Chem. C* **2017**, *121*, 3503.
[23] R. G. Geitenbeek, J. C. Vollenbroek, H. M. H. Weijgertze, C. B. M. Tregouet, A. E. Nieuwelink, C. L. Kennedy, B. M. Weckhuysen, D. Lohse, A. van Blaaderen, A. van den Berg, M. Odijk, A. Meijerink, *Lab Chip* **2019**, *19*, 1236.
[24] T. P. van Swieten, T. van Omme, D. J. van den Heuvel, S. J. W. Vonk, R. G. Spruit, F. Meirer, H. H. P. Garza, B. M. Weckhuysen, A. Meijerink, F. T. Rabouw, R. G. Geitenbeek, *ACS Appl. Nano Mater.* **2021**, *4*, 4208.
[25] I. K. van Ravenhorst, R. G. Geitenbeek, M. J. van der Eerden, J. T. van Omme, H. H. Peréz Garza, F. Meirer, A. Meijerink, B. M. Weckhuysen, *ChemCatChem* **2019**, *11*, 5505.
[26] Y. Gao, Y. Bando, *Nature* **2002**, *415*, 599.
[27] N. W. Gong, M. Y. Lu, C. Y. Wang, Y. Chen, L. J. Chen, *Appl. Phys. Lett.* **2008**, *92*, 2006.
[28] M. Mecklenburg, W. A. Hubbard, E. R. White, R. Dhall, S. B. Cronin, S. Aloni, B. C. Regan, *Science* **2015**, *347*, 629.
[29] S. B. Vendelbo, P. J. Kooyman, J. F. Creemer, B. Morana, L. Mele, P. Dona, B. J. Nelissen, S. Helveg, *Ultramicroscopy* **2013**, *133*, 72.
[30] J. C. Idrobo, A. R. Lupini, T. Feng, R. R. Unocic, F. S. Walden, D. S. Gardiner, T. C. Lovejoy, N. Dellby, S. T. Pantelides, O. L. Krivanek, *Phys. Rev. Lett.* **2018**, *120*, 95901.
[31] M. J. Lagos, P. E. Batson, *Nano Lett.* **2018**, *18*, 4556.
[32] A. Takaoka, K. Ura, *J. Electron Microsc.* **1990**, *39*, 69.
[33] J. P. Winterstein, P. A. Lin, R. Sharma, *Microsc. Microanal.* **2015**, *21*, 1622.
[34] E. Kano, M. Malac, M. Hayashida, *Carbon* **2020**, *163*, 324.
[35] F. Niekiel, S. M. Kraschewski, J. Müller, B. Butz, E. Spiecker, *Ultramicroscopy* **2017**, *176*, 161.
[36] J. E. S. van der Hoeven, T. S. Deng, W. Albrecht, L. A. Olthof, M. A. van Huis, P. E. de Jongh, A. van Blaaderen, *ACS Omega* **2021**, *6*, 7034.
[37] W. Albrecht, T. S. Deng, B. Goris, M. A. van Huis, S. Bals, A. van Blaaderen, *Nano Lett.* **2016**, *16*, 1818.
[38] T. K. Moon, **1996**, *13*, 47–60.
[39] W. van Aarle, W. J. Palenstijn, J. de Beenhouwer, T. Altantzis, S. Bals, K. J. Batenburg, J. Sijbers, *Ultramicroscopy* **2015**, *157*, 35.
[40] D. B. Williams, C. B. Carter, *Transmission Electron Microscopy*, Springer, New York **2009**, https://doi.org/10.1007/978-1-4757-2519-3_6.
[41] W. C. Mallard, A. B. Gardner, R. F. Bass, L. M. Slifkin, *Phys. Rev.* **1963**, *129*, 617.
[42] M. A. Noah, D. Flötotto, Z. Wang, M. Reiner, C. Hugenschmidt, E. J. Mittemeijer, *Acta Mater.* **2016**, *107*, 133.
[43] M. Mychinko, A. Skorikov, W. Albrecht, A. Sánchez-Iglesias, X. Zhuo, V. Kumar, S. Bals, *Small* **2021**, *17*, 2102348.
[44] X. C. Ye, C. Zheng, J. Chen, Y. Z. Gao, C. B. Murray, *Nano Lett.* **2013**, *13*, 765.
[45] I. Gorelikov, N. Matsuura, *Nano Lett.* **2008**, *8*, 369.
[46] J. E. S. van der Hoeven, T. A. J. Welling, T. A. G. Silva, J. E. van den Reijen, C. L. Fontaine, X. Carrier, C. Louis, A. van Blaaderen, P. E. de Jongh, *ACS Nano* **2018**, *12*, 8467.
[47] P. Virtanen, R. Gommers, T. E. Oliphant, M. Haberland, T. Reddy, D. Cournapeau, E. Burovski, P. Peterson, W. Weckesser, J. Bright, S. J. van der Walt, M. Brett, J. Wilson, K. J. Millman, N. Mayorov, A. R. J. Nelson, E. Jones, R. Kern, E. Larson, C. J. Carey, İ. Polat, Y. Feng, E. W. Moore, J. VanderPlas, D. Laxalde, J. Perktold, R. Cimrman, I. Henriksen, E. A. Quintero, C. R. Harris, et al., *Nat. Methods.* **2020**, *17*, 261.